applied sciences

MDPI

Article

Radon Exhalation Rate, Radioactivity Content, and Mineralogy Assessment of Significant Historical and Artistic Interest Construction Materials

Francesco Caridi [1,*], Daniele Chiriu [2], Stefania Da Pelo [3], Giuliana Faggio [4], Michele Guida [5], Giacomo Messina [4], Maurizio Ponte [6], Silvestro Antonio Ruffolo [6], Domenico Majolino [1] and Valentina Venuti [1]

[1] Dipartimento di Scienze Matematiche e Informatiche, Scienze Fisiche e Scienze della Terra, Università degli Studi di Messina, V.le F. Stagno D'Alcontres, 31, 98166 Messina, Italy; dmajolino@unime.it (D.M.); vvenuti@unime.it (V.V.)
[2] Dipartimento di Fisica, Università degli Studi di Cagliari, Cittadella Universitaria di Monserrato, S.P. Monserrato-Sestu Km 0,700, 09042 Monserrato, Italy; daniele.chiriu@dsf.unica.it
[3] Dipartimento di Scienze Chimiche e Geologiche, Università degli Studi di Cagliari, Cittadella Universitaria di Monserrato, S.P. Monserrato-Sestu Km 0,700, 09042 Monserrato, Italy; sdapelo@unica.it
[4] Dipartimento di Ingegneria dell'Informazione, delle Infrastrutture e dell'Energia Sostenibile (DIIES), Università "Mediterranea", Via Zehender, 89122 Reggio Calabria, Italy; gfaggio@unirc.it (G.F.); messina@unirc.it (G.M.)
[5] Dipartimento di Ingegneria dell'Informazione ed Elettrica e Matematica applicata (DIEM), Università Degli Studi di Salerno, Via Giovanni Paolo II, 132, 84084 Fisciano, Italy; miguida@unisa.it
[6] Dipartimento di Biologia, Ecologia e Scienze della Terra (DiBEST), Università della Calabria, Via Pietro Bucci, 87036 Arcavacata di Rende, Italy; maurizio.ponte@unical.it (M.P.); silvestro.ruffolo@unical.it (S.A.R.)
* Correspondence: fcaridi@unime.it

Abstract: In this paper, an investigation focused on assessing the radon exhalation, the natural radioactivity level, and the mineralogy of natural stones of particular historical–artistic interest employed as building materials was carried out. The Closed Chamber Method (CCM) with the Durridge Rad7 apparatus for short-lived radon progeny alpha spectrometry and High Purity Germanium (HPGe) gamma spectrometry were used to determine the radon exhalation rate and specific activities of ^{226}Ra, ^{232}Th, and ^{40}K, respectively. Furthermore, several indices were evaluated to determine the radiological risk due to radiation exposure from the investigated natural stones, i.e., the absorbed gamma dose rate (D), the activity concentration index (ACI), and the alpha index (I_α). Finally, X-ray diffraction (XRD) and Micro-Raman Scattering (MRS) investigations were performed to correlate the chemical composition and mineralogical characteristics of natural stones with the radon exhalation rate and the natural radioactivity content. It is worth noting that the findings from this study can be used to guide future research into the background levels of radioactivity in stones used as construction materials.

Keywords: building materials; radioactivity; radiological risk; radon exhalation; mineralogy

Citation: Caridi, F.; Chiriu, D.; Pelo, S.D.; Faggio, G.; Guida, M.; Messina, G.; Ponte, M.; Ruffolo, S.A.; Majolino, D.; Venuti, V. Radon Exhalation Rate, Radioactivity Content, and Mineralogy Assessment of Significant Historical and Artistic Interest Construction Materials. *Appl. Sci.* **2024**, *14*, 11359. https://doi.org/10.3390/app142311359

Academic Editor: Lola Pereira

Received: 8 November 2024
Revised: 29 November 2024
Accepted: 3 December 2024
Published: 5 December 2024

1. Introduction

In light of the presence of cosmogenic radionuclides and primordial radioisotopes in the Earth's crust, environmental natural radioactivity is the main cause of the population's exposure to ionizing radiations [1]. Nuclides from the radioactive chains of ^{238}U, ^{232}Th, ^{235}U, and primordial ^{40}K are noteworthy from the viewpoint of natural radioactivity [2]. Common environmental matrices holding these naturally occurring radioisotopes include water, soil, and rocks [3,4], the last of which can be used as materials for construction. Thus, investigations on the amount of naturally occurring radioactivity in rocks offer crucial instruments for assessing the radiological risk that humans face from ionizing radiation exposure [5]. This endeavor becomes critical because, as the literature states [6],

prolonged exposure to uranium and radium can result in various health effects, such as acute leucopoenia, anemia, oral necrosis, and chronic lung diseases; on the other hand, exposure to thorium can lead to leukemia and cancers of the pancreas, liver, kidney, lung, and brain [7]. Additionally, chronic exposure to radon gas (^{222}Rn) may increase the risk of lung cancer [8]. Indeed, only smoking in the general population is a greater risk factor for lung cancer than radon and its daughters, according to the World Health Organization (WHO) [9,10]. Therefore, it is crucial to continue keeping surveillance on the amounts of radon and its progeny in the environment in order to assess the threats to human health associated with the radiological risks [11]. Although construction materials with large activities of ^{226}Ra may represent another important source of natural radiation [12], given that ^{226}Ra decays to ^{222}Rn in the ^{238}U decay chain, the pressure-driven influx from subterranean soil is the primary source of indoor radon. Radium and/or uranium traces range from 2 to 4 parts per million (background) to 1000 parts per million (black shales) in various types of rocks [13]. Within the category of igneous rocks, crystalline rocks with a higher probability of containing uranium include granites, granitic pegmatites, and syenites [14]. In these rocks, trace minerals such as zircon, monazite, and allanite contain most of the uranium/radium content [15]. The exhalation of ^{222}Rn from a particular rock surface is significantly influenced by the petrographic and petrophysical properties of the rock itself, even if studies of U/Ra activity might provide useful information on radon release potential [16]. Therefore, to determine the actual risk associated with a particular natural stone, real-time measurements of ^{222}Rn emission rates are required [17]. Lastly, geochemical analyses of rocks can shed light on elemental distribution patterns, which are then connected to the current environmental state of a particular region [18].

In this framework, a multidisciplinary approach was used in this work to determine the activity concentration of natural radionuclides in stone samples of particular historical–artistic interest from Noto, Comiso, and Mendicino, Southern Italy, presented as a case study. The results were then correlated with the mineralogy and geochemistry of the samples. In the study locations, they were mostly employed as building materials [19]. Several analytical techniques were used in the multidisciplinary approach, including the Closed Chamber Method (CCM) [20] with the Durridge Rad7 apparatus for short-lived radon progeny alpha spectrometry, High Purity Germanium detector (HPGe), X-ray diffraction (XRD), and Micro-Raman Scattering (MRS) spectroscopy. To calculate the possible danger to radiological health associated with radiation exposure from the investigated rocks, further calculations were made to evaluate the absorbed gamma dose rate (D), activity concentration index (ACI), and alpha index (I_α).

2. Geological Framework of the Investigated Samples

The Palazzolo Formation limestone, also called "Noto stone" was widely used in Sicilian Baroque monuments. It is locally called "carving stone", because it is easy to carve and, once exposed, it changes from a pale yellow color to a golden appearance [21]. The Palazzolo Formation has extensive outcrops in the Hyblean Plateau, in Southeastern Sicily, that represents a forebulge, a result from the bending of the African continental foreland lithosphere underneath the advancing Maghrebian thrust-fold belt. Moreover, belonging to the eastern Oligocene–Miocene palaeogeographic domain of the Cretaceous–Quaternary succession of the Hyblean plateau, it consists of shallow-water algal-bryozoan thick-bedded calcarenites overlying Cretaceous reefal to lagoonal rudist limestones with intercalated pyroclastic rocks in the northeast [21]. The Palazzolo Formation, which is in transitional contact with the marls of the Tellaro Formation, can be divided into two members: the Gaetanì and Buscemi members, the lower and upper part, respectively. They are characterized by heteroplastic relations, especially towards the east, where the Buscemi Formation is most represented. The recognized lithofacies are: (i) one consists of fine-grained gray limestones and soft marly limestones alternating in 20–40 cm thick beds and (ii) the other is characterized by yellowish-white limestones exposed in large bank levels.

Comiso stone belongs to the lower Leonardo Member (upper Oligocene) of the Ragusa Formation (upper Oligocene–Miocene) in the Hyblean area, which is formed of alternating calcareous and marly layers. This stone, mainly made of calcite, well lithified, white-cream and fine-grained calcarenite, with tenacious consistency and homogeneous structure is collected in Eastern Sicily and was largely used in the monuments of the Baroque cities of the "Val di Noto" (i.e., Catania, Siracusa, Noto, Ragusa, and Modica) included in the UNESCO's World Heritage List, which were completely destroyed following the earthquake of 1693 [22].

The Comiso stone's outcropping can be found near the Comiso Chiaramonte System that stretches all the way to the Monterosso Almo hamlet and divides a raised area to the southeast where Oligo–Miocene limestones are found. The three main SW-NE trending, left-stepping en-echelon, dextral strike-slip faults—the Comiso, Chiaramonte, and Monterosso faults—form the SSW-NNE oriented shear zone that characterizes the structural setting. Pliocene volcanics and lower Pleistocene calcarenites predate the Comiso–Chiaramonte–Monterosso fault zone's period of deformation, while middle Pleistocene alluvial deposits postdate it. In response to the same stress field that caused the partial reactivation of Neogene normal faults with right-lateral strike-slip displacements and the neoformation of associated structures, characterized by the over-stepping geometry of the main faults, the fault system developed concurrently with the well-known Sicily–Ragusa dextral wrench zone, also oriented SSW-NNE, according to the simple shear model. Because of this, the Comiso–Chiaramonte–Monterosso fault zone and the Sicily–Ragusa system can be viewed as the onshore extension of the SSW-NNE directed transform zone that allowed the Pantelleria Rift to extend during the Plio-Pleistocene in the Strait of Sicily [23].

The "Calcare di Mendicino" is a part of the Tortonian–Messinian sedimentary succession that represents the infilling of the basins opened during the lower Tortonian in the western area of the Calabrian Arc. It is characterized by a clastic marine sequence that unconformably overlies the Paleozoic bedrock, dipping outward concerning the massif [24]. These deposits are further overlain in an unconformable manner by transgressive marine deposits from the upper Pliocene to the lower Pleistocene. In the western region of the Calabrian Arc, the forearc belt associated with the active subduction of the Ionian Basin, the filling of the basins formed during the lower Tortonian is described. Within half-graben structures like the Crati Valley and along the western slope of the Coastal Range (Catena Costiera), the Tortonian–Messinian succession manifests as sporadic relics that are periodically displaced to altitudes of up to 900 m above sea level [25]. The age of the "Calcare di Mendicino" was established using the planktonic foramniferal faunal assemblage of the underlying and overlying clayey strata. Four main lithostratigraphic units that are laterally correlated over a large area can be distinguished within the succession [25].

3. Materials and Methods

Five aliquots for each one of the investigated "Noto", "Comiso", and "Mendicino" natural stones were obtained by cutting at the laboratory larger pieces of stones by means of a circular saw. Each aliquot was a cube of approximately 5 cm.

3.1. Radon Exhalation Rate Measurements

The radon exhalation rate of each aliquot of the analyzed natural stones was assessed by using the Closed Chamber Method (CCM) [26]. In particular, the experimental set-up consists of a small cylindric steel vessel (volume 2.75 L) connected with the Durridge Rad7 instrument [27], a drying unit filled with desiccant ($CaSO_4$), and some vinyl tubes making a closed air circuit (see Figure 1).

Figure 1. A photo of the experimental set-up for the radon exhalation assessment.

The radon-rich air enters the stainless-steel measuring chamber after passing through the drying unit and the inlet filter (which avoids the entrance of dust and the electrically charged radon progeny), is aspired by the internal pump, and then is expelled outside the chamber through the output (outlet), forming a closed air loop. Inside the chamber, the filtered air decays and releases detectable alpha-emitting progeny, including polonium isotopes. The chamber walls are subjected to a high voltage of 2500 V. The Rad7 solid-state silicon detector (Rad7 (Durridge, Billerica, MA, USA)) distinguishes between the electrical pulses produced by α-particles coming from ^{218}Po, ^{216}Po, ^{214}Po, and ^{212}Po (progeny of ^{222}Rn and ^{220}Rn), with energies of 6 MeV, 6.7 MeV, 7.7 MeV, and 8.8 MeV, respectively, by directly converting alpha radiation to an electrical output.

Since the equilibrium between ^{218}Po and ^{222}Rn is reached in roughly 15 min (almost five times the half-life of ^{218}Po), it is possible to employ solely the ^{218}Po activity concentration for ^{222}Rn, achieving a rapid equilibrium between polonium and radon nuclei [28].

The radon growth curve to equilibrium was monitored over a period of 10 days and the ^{222}Rn specific exhalation rate, E (Bq h^{-1} kg^{-1}), was calculated according to the following equation [26]:

$$E = \frac{(C - C_0 e^{-\lambda T})/m}{1 - e^{-\lambda T}} \lambda V \quad (1)$$

where C is the equilibrium concentration (Bq m^{-3}); C_0 is the initial radon concentration (Bq m^{-3}); λ (h^{-1}) is the effective decay constant and is defined as a sum of radon decay constant, back diffusion, and the leakage constant [29]; V is the total volume of the analytical system (m^3); T is time of exposure (240 h); and m is the mass of the sample (kg). In order to reduce the leakage from the chamber, an insulating rubber was employed [30].

3.2. HPGE γ-Spectrometry Set-Up

For the HPGe γ-spectrometry analysis, each aliquot of the investigated samples was first powdered then dried at 105 °C in an oven for 24 h to completely remove moisture and finally inserted in a Marinelli container of 1 L capacity. After 40 days, the secular radioactive equilibrium between ^{226}Ra and its daughter radionuclides was reached, and samples were ready for γ-spectrometry counting [31].

In addition, samples were counted for 70,000 s to reduce the statistical uncertainty, and spectra were analyzed to assess the specific activity of ^{226}Ra, ^{232}Th, and ^{40}K. In particular, the ^{226}Ra-specific activity was quantified through the 295.21 keV and 351.92 keV ^{214}Pb and 1120.29 keV ^{214}Bi γ-ray lines, respectively, and the ^{232}Th-specific activity was determined

by using the 911.21 keV and 968.97 keV ^{228}Ac γ-ray lines. For ^{40}K, the evaluation was performed from its γ-line at 1460.8 keV [32].

The true coincidence summing corrections (TCC) was not carried out for the photopeak of ^{214}Bi nor for the 911.21 keV ^{228}Ac γ-ray line because it fell within the counting uncertainty. Moreover, the correction due to the interference of ^{228}Ac in the photopeak of ^{40}K was not performed because the concentration of the ^{232}Th series was very low and such influence was not produced.

Table 1 reports the operating parameters of the employed detector.

Table 1. The negative biased Ortec HPGe detector operating parameters.

Negative Biased Ortec HPGe Detector	
FWHM	1.94 keV
Peak to Compton ratio	65:1
Relative efficiency	37.5% (at the 1.33 MeV ^{60}Co γ-line)
Bias voltage	−4800 V
Energy range	5 keV–2 MeV

The sample was installed into lead sumps to screen off background ambient radiation. It is worthy to note that efficiency and energy calibrations were carried out for the 1 L sample holder shape using Eckert and Zigler Nuclitec GmgH traceable multinuclide radioactive standard, number AK-5901 [33]. The Gamma Vision (Ortec) software version 8 was used for data acquisition and analysis [34].

The activity concentration (Bq kg^{-1} dry weight, d.w.) of the investigated radioisotopes was given by [35] as follows:

$$C(Bqkg^{-1}d.w.) = \frac{N_E}{\varepsilon_E t \gamma_d M} \quad (2)$$

where N_E indicates the net area of a peak at energy E; ε_E and γ_d are the efficiency and yield of the photopeak at energy E, respectively; M is the mass of the sample (kg); and t is the live time (s) [36].

The quality of the HPGe gamma spectrometry results was certified by the Italian Accreditation Body (ACCREDIA) on the basis of the quality controls performed according to the UNI 11665:2017 [37].

3.3. Evaluation of Radiological Hazard Effects

3.3.1. Absorbed Gamma Dose Rate

The absorbed gamma dose rate, D (nGy h^{-1}), for the indoor external exposure was first used to quantify the radiological health risk. This rate was computed using the standard room model, as stated in [38].

$$D = 0.92C_{Ra} + 1.1C_{Th} + 0.08C_K \quad (3)$$

where C_{Ra}, C_{Th}, and C_K are the average activity concentrations (the mean value of the five analyzed aliquots) of ^{226}Ra, ^{232}Th, and ^{40}K in the analyzed samples, respectively.

3.3.2. Activity Concentration Index

The European Commission established the following activity concentration index (ACI) to determine if the dose criterion is satisfied [39]:

$$ACI = (C_{Ra}/300 + C_{Th}/200 + C_K/3000) \quad (4)$$

It relates to the reference limit of 1 mSv y^{-1} that applies to both the external and indoor exposure to gamma radiation emitted by building materials, in addition to the outdoor

exposure [40]. Therefore, the only application for this index would be as a screening tool to identify materials that might be dangerous when used in buildings. Refrain from those with I > 1, as these values indicate exposure rates greater than 1 mSv y^{-1}.

3.3.3. Alpha Index

The alpha index was given by [41] as follows:

$$I_\alpha = C_{Ra}/200 \quad (5)$$

It assesses the alpha radiation exposure to the indoor radon emitted by building materials. To avoid exposure to the indoor radon activity over the threshold of 200 Bq m^{-3}, the activity concentration of ^{226}Ra must be less than 200 Bq kg^{-1}. Thus, I_α must be less than 1 to minimize radiation exposure risk [42].

3.4. X-Ray Diffraction (XRD) Set-Up

X-ray diffraction analyses were conducted by using a Panalytical Empyrean Diffractometer equipped with Cu Kα radiation and a Bragg–Brentano theta–theta goniometer, utilizing a solid-state PIXcel detector [43]. Approximately 1 g of a finely powdered sample of natural stones was employed for each analysis. The acquisition settings were 40 kV and 40 mA, with XRD patterns recorded over a 2θ range from 2° to 70°, employing a step size of 0.007° and a counting time of 20 s. To remove the Cu Kα2 component, the raw data were processed using software correction, while the background was corrected using a digital filter. The observed peak positions were compared against the ICDD JCPDS database to identify the crystalline mineral components present in the analyzed natural stones [44].

3.5. Micro-Raman Scattering (MRS) Measurements

Micro-Raman Scattering (MRS) measurements were collected on the investigated stones using a portable "BTR111MiniRam™" (BW&TEK Inc., Newark, NJ, USA) spectrometer. The instrument works with a 785 nm (diode laser) excitation wavelength and a thermoelectric cooled charge-coupled device (CCD) detector. The system was supplied with a BAC151B Raman microscope [45]. The laser spot was focused on the surface through a 40×/80× objective, which assured a working distance of 3.98 mm and a laser beam spot size of 50/25 µm. In our case, a maximum laser power at the samples of ~90 mW was delivered. The spectra were registered in a wavenumber range between 60 and 3150 cm^{-1} by using an acquisition time of 10 s and a resolution of 8 cm^{-1}. To increase the signal–to–noise ratio, 18 scans were accumulated. Prior to each measurement, the device was calibrated using a silicon chip's peak at 520.6 cm^{-1} to ensure optimal performance [46].

4. Results and Discussion

4.1. Radon Exhalation and Radioactivity Analysis

The most representative radon growth curves to equilibrium are shown in Figure 2 for the "Noto" (a), "Comiso" (b), and "Mendicino" (c) natural stones, respectively.

The fitted effective decay constant is reported in the graphs. A comparison between its values, i.e., (0.020 ± 0.003) h^{-1}, (0.050 ± 0.003) h^{-1}, and (0.081 ± 0.011) h^{-1}, for the Noto, Comiso, and Mendicino natural stones, respectively, and the radon decay constant, i.e., 0.008 h^{-1}, demonstrate that the bound exhalation and the leakage cannot be neglected as their contribution is equal to about 0.012 h^{-1}, 0.042 h^{-1}, and 0.073 h^{-1}, for the Noto, Comiso, and Mendicino samples, respectively.

Table 2 reports the average ^{222}Rn-specific exhalation rate (the mean value for the five aliquots of the investigated rocks) for all the analyzed natural stones.

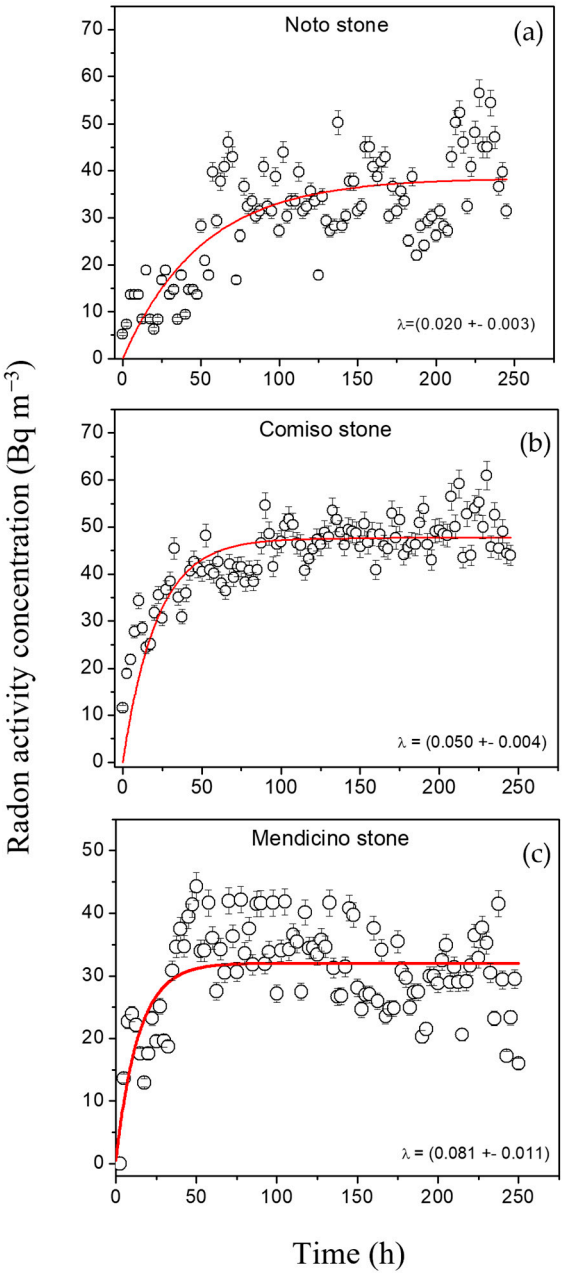

Figure 2. The most representative radon growth curves to equilibrium for the "Noto" (**a**), "Comiso" (**b**), and "Mendicino" (**c**) natural stones.

Table 2. The average ^{222}Rn-specific exhalation rate for the analyzed natural stones.

Sample	^{222}Rn Exhalation Rate (Bq h^{-1} kg^{-1})
Noto stone	0.013 ± 0.003
Comiso stone	0.040 ± 0.006
Mendicino stone	0.030 ± 0.010

It is worth noting that, by making the requisite schematic assumptions and utilizing the findings of the radon exhalation measurements, it is feasible to calculate the impact of a specific stone, hypothesized to be employed in the confinement of a defined volume on the accumulation of radon within an indoor environment. The indoor radon concentration

resulting from the confining walls can be readily estimated as reported in [47], and it was found to be lower than 10 Bq m^{-3} for all investigated natural stones. The air exchange rate of 0.2 h^{-1} was assumed [47].

Moreover, the ^{226}Ra, ^{232}Th, and ^{40}K mean activity concentrations (the average value across the five aliquots of the rocks under study) for the investigated samples are reported in Table 3.

Table 3. ^{226}Ra, ^{232}Th, and ^{40}K average activity concentrations for analyzed natural stones.

Sample	Activity Concentration		
	C_{Ra} (Bq kg^{-1})	C_{Th} (Bq kg^{-1})	C_K (Bq kg^{-1})
Noto stone	14.5 ± 1.6	0.99 ± 0.16	6.2 ± 0.8
Comiso stone	21.9 ± 1.9	1.8 ± 0.3	3.2 ± 0.4
Mendicino stone	8.6 ± 0.7	9.4 ± 0.8	169 ± 23

It is important to point out that, in all cases, the activity concentrations of ^{226}Ra, ^{232}Th, and ^{40}K are significantly lower than the average world values, i.e., 35 Bq kg^{-1}, 30 Bq kg^{-1}, and 400 Bq kg^{-1}, respectively [48]. According to published research, the chemical composition and mineralogical characteristics of natural stones have a significant impact on the values of the ^{222}Rn exhalation rate, as well as C_{Ra}, C_{Th}, and C_K [49,50]. For this reason, further investigations about the chemical and mineralogical composition of the investigated "Noto", "Comiso", and "Mendicino" stones through Micro-Raman Scattering and X-ray diffraction were carried out, as detailed in the following section.

4.2. Evaluation of Radiological Health Risks

Table 4 reports D, ACI, and I_α, as calculated by using Equations (3)–(5).

Table 4. The absorbed gamma dose rate (D), the activity concentration index (ACI), and the alpha index (I_α) for the investigated samples.

Sample	D (nGy h^{-1})	ACI	I_α
Noto stone	14.9	0.06	0.07
Comiso stone	22.4	0.08	0.11
Mendicino stone	31.8	0.13	0.04

It is worthy to note that the absorbed gamma dose rate for the examined samples can be attributed to the lithologic component of the sampling location, as widely documented in the literature [51]. It was found to be lower than the natural background value of 59 nGy h^{-1} in all cases [52].

Moreover, the investigated natural stones' potential as building materials was then assessed by calculating their activity concentration index. It turned out to be 0.06, 0.08, and 0.13 for the "Noto", "Comiso", and "Mendicino" rocks, respectively, which are much lower than 1, showing insignificant radiological risks connected to the gamma radiation exposure. Finally, the alpha index value was determined to be 0.07, 0.11, and 0.04 for the "Noto", "Comiso", and "Mendicino" stones, respectively, preventing exposure to indoor radon activity concentrations exceeding 200 Bq m^{-3}.

4.3. XRD Analysis

The most representative XRD spectrum for the "Noto" stone is shown in Figure 3.

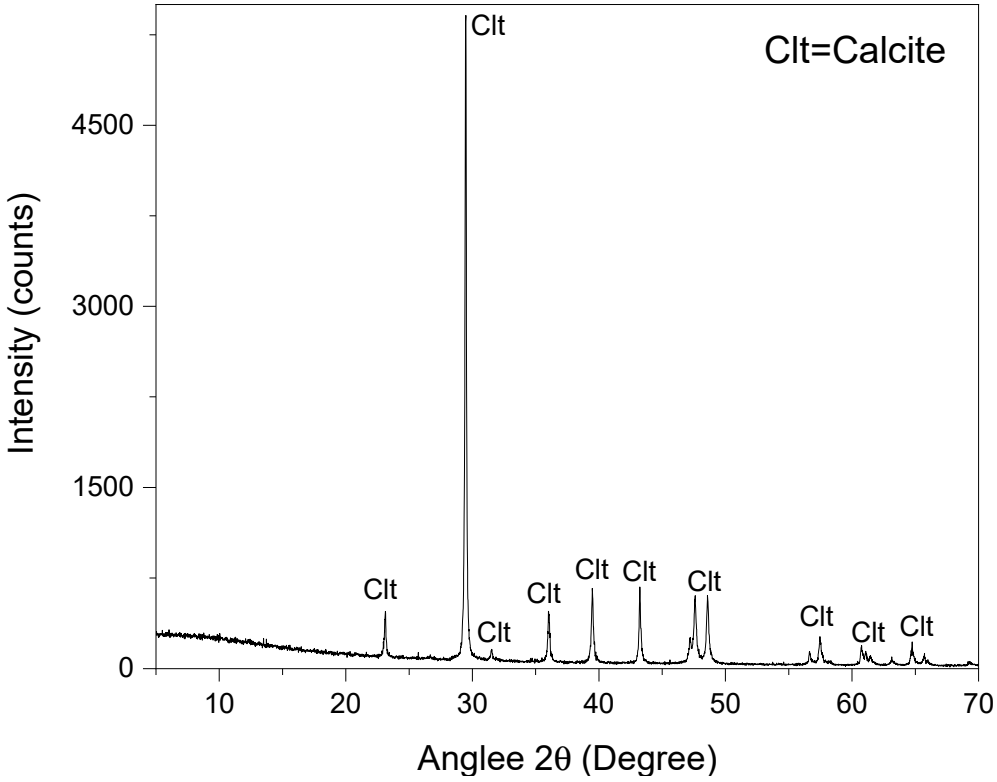

Figure 3. XRD pattern of Noto specimen. Prominent peaks attributed to calcite mineral.

The crystalline mineral phases were determined by correlating the measured diffraction peak positions with the ICDD JCPDS database.

The XRD spectrum reveals clear evidence of a dominant crystalline phase. The labeled peaks, all identified as calcite (Clt), highlight the presence of this mineral as the primary component in the sample. The most intense peak at approximately 29.5° 2θ, corresponding to the main reflection plane of calcite, indicates its high abundance. This condition is typical for calcite-dominated materials, as this peak is associated with the (104) plane, which produces the strongest reflection in calcite due to its crystallographic orientation. In addition, smaller but well-defined peaks are also observed between 20° and 70° 2θ, with characteristic positions confirming calcite as the only significant crystalline phase. These additional peaks further reinforce the conclusion that calcite is the principal mineral, and the uniform intensity and sharpness of these reflections suggest a highly ordered, well-crystallized structure. The lack of any notable peaks or secondary phases suggests that this sample is largely free from impurities, reinforcing the high purity of the calcite in the "Noto" natural stone. The uniformity of the diffraction peaks, coupled with the absence of significant noise, indicates that the sample likely has a homogenous structure without significant mineralogical variation. Thus, the XRD analysis strongly confirms that calcite is the only crystalline mineral present in the sample. The presence of sharp, well-defined peaks and the high intensity of the main calcite reflection identified a high-quality, well-crystallized stone with minimal impurities. The structural uniformity of the "Noto" stone make it more appreciated in architectural and ornamental applications, owing to its mechanical strength and visual appeal [53].

Moreover, Figure 4 reports the most representative XRD spectrum for the "Comiso" stone.

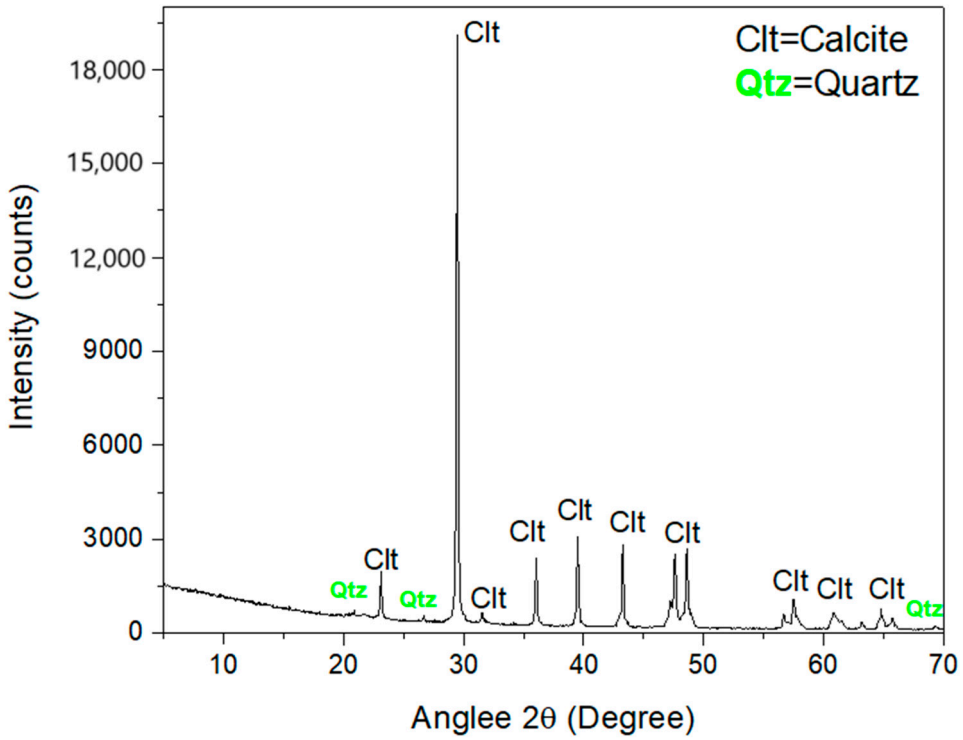

Figure 4. XRD pattern of Comiso specimen, with prominent peaks attributed to calcite (Clt) and quartz (Qtz).

The XRD pattern reveals two primary crystalline phases: calcite (Clt) and quartz (Qtz). Calcite is the predominant mineral, with its strongest diffraction peak occurring around 29.5° 2θ, corresponding to the (104) plane, indicating a high concentration of calcite. Multiple additional calcite peaks between 20° and 70° further confirm its dominance in the sample. The smaller peaks identified at 2θ values around 20.8°, 26.6°, and 68° and the intensity of these reflections indicates that quartz is a secondary phase; however, its identification contributes to the mineralogical composition of the "Comiso" stone. The sharpness of the calcite and quartz peaks indicates a well-crystallized structure, suggesting that the minerals within the sample have undergone minimal weathering or alteration, preserving their crystalline integrity. The combination of calcite and quartz in the sample is coherent with the typical mineralogical composition of limestones, particularly those from the Comiso area, which are often characterized by high calcite content with minor siliceous impurities. This composition enhances the stone's workability and esthetic appeal, making it highly desirable for architectural uses [54]. The purity of the specimen is notable, as no other significant crystalline phases were detected. This supports the conclusion that the "Comiso" stone is primarily composed of calcite with a small but notable quartz content. Such a composition has been documented in studies focusing on the properties of Comiso limestone, confirming its suitability for both structural and decorative purposes [54]. The XRD analysis confirms that the mineralogical composition of this sample is mainly calcitic, with quartz identified as a secondary phase. The well-crystallized structure and the lack of other mineral phases indicate its high purity, which makes it suitable for a variety of construction and ornamentation applications due to its beneficial mineralogical and mechanical properties [53].

Finally, the most representative XRD spectrum for the "Mendicino" stone is shown in Figure 5.

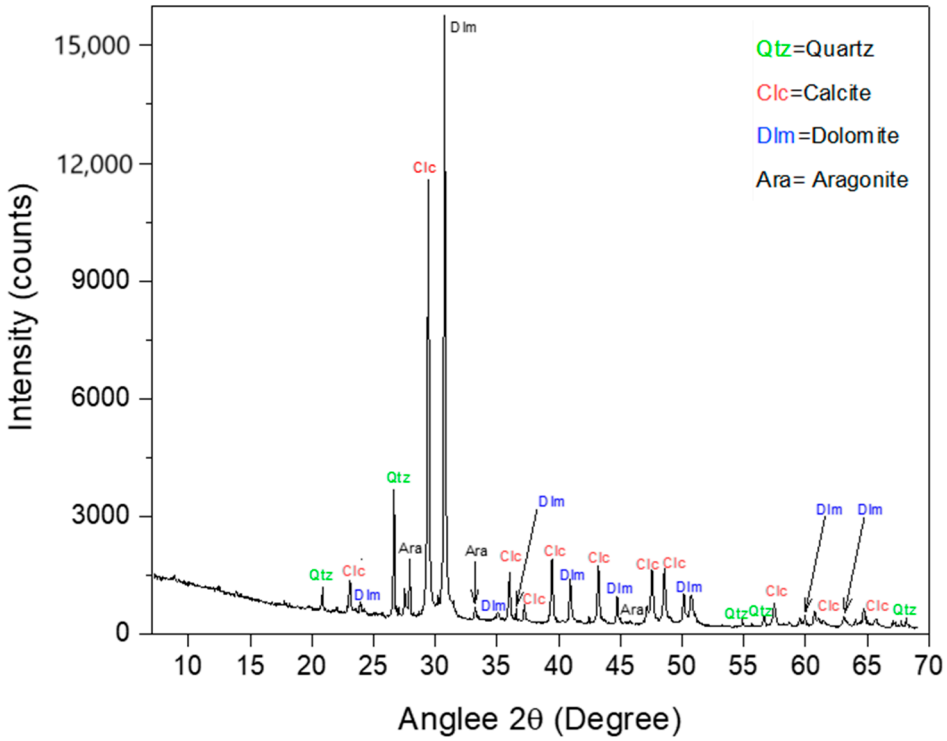

Figure 5. XRD pattern of Mendicino specimen. Detected minerals include quartz, calcite, dolomite, and aragonite.

The XRD analysis reveals a complex mineral composition with several distinct crystalline phases. The most prominent peaks correspond to dolomite, calcite, quartz, and aragonite. Dolomite is one of the most significant components, as indicated by the high-intensity peaks near 30° and 65° 2θ. This suggests that dolomite is the most abundant mineral in the stone, contributing to its structural characteristics. The presence of calcite is also notable, with peaks around 23°, 29°, and 47°, signifying its role as a key carbonate mineral in the sample. Calcite often coexists with dolomite in sedimentary rocks, further confirming the geological origin of the stone. The diffraction peaks of quartz, a silicate mineral, are shown at 26.7° and 50°, with minor intensity compared to the carbonate minerals. Quartz's presence can be attributed to its durability and widespread occurrence in natural stone formations, where it provides hardness and resilience. Aragonite, a polymorph of calcium carbonate, is identified with lower intensity peaks around 26° and 45°, suggesting it is present in smaller quantities. Its formation could be related to diagenetic processes that occurred during the stone's geological history, possibly impacted by regional climatic factors including pressure and temperature. The combination of these minerals points to a sedimentary origin for the Mendicino stone, likely formed through processes of compaction and the recrystallization of carbonate-rich sediments [25]. The prevalence of dolomite and calcite, both common in limestones and dolostones, further supports this hypothesis. Additionally, the presence of quartz suggests that siliciclastic material was incorporated during the stone's formation, enhancing its mechanical properties. These results are consistent with findings from similar studies on carbonate stones [55]. The coexistence of dolomite and calcite in natural stones is a common feature of many geological formations, particularly those originating from marine environments where carbonate deposition is prevalent. Additionally, as reported in [56], the aragonite can form under certain conditions of supersaturation in marine environments, further supporting the sedimentary origin of the "Mendicino" stone.

It is worthy to note that the observed discrepancy in activity levels between uranium and thorium in the investigated samples can be directly attributed to the geochemical behavior and compatibility of these elements with the calcite crystalline structure. Uranium,

predominantly present as the uranyl ion (UO_2^{2+}) under oxidizing conditions, exhibits high compatibility with calcite, where it can substitute calcium (Ca^{2+}) through ionic substitution mechanisms. This incorporation is facilitated by the similarity in ionic radii and charge between UO_2^{2+} and Ca^{2+}. In contrast, thorium, which predominantly exists as Th^{4+}, has significantly lower solubility in aqueous environments and reduced compatibility with calcite, limiting its incorporation.

These observations align with prior studies. In particular, Finch and Murakami detailed the mechanisms of uranium incorporation into carbonates, highlighting the preferential affinity of uranyl ions for carbonate minerals under near-surface conditions [57]. Similarly, Langmuir [58] and Ivanovich and Harmon [59] demonstrated the role of geochemical speciation and mineral-matrix compatibility in explaining the disparity between uranium and thorium uptake. Therefore, our findings confirm that the higher uranium activity in calcite reflects these established geochemical principles.

4.4. MRS Analysis

The micro-Raman spectra reported in Figures 6–8 for the "Noto", "Comiso", and "Mendicino" stones, respectively, are representative of 15 different measurements collected on different spots of the surface exhibiting similar profiles, in the wavenumber range between 100 cm^{-1} and 2000 cm^{-1}.

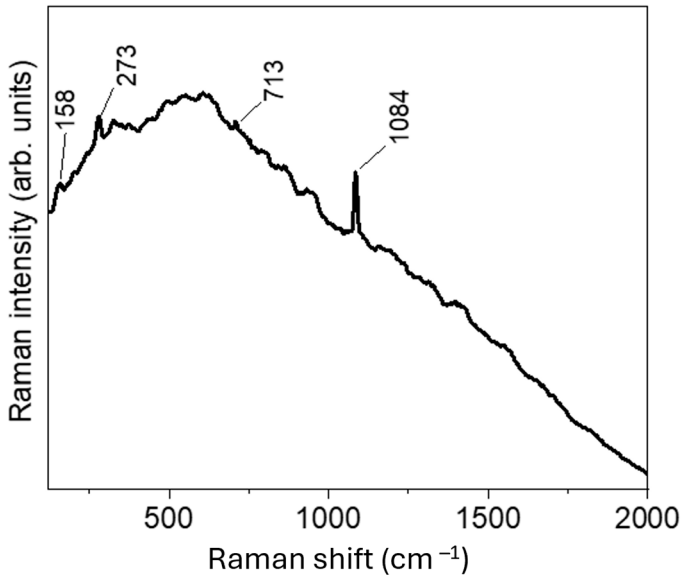

Figure 6. Representative micro-Raman spectrum recorded on the "Noto" stone in the wavenumber range between 100 cm^{-1} and 2000 cm^{-1}.

Furthermore, for the "Noto" stone, the detected micro-Raman profile shown in Figure 6 revealed the typical vibrational peaks of calcite ($CaCO_3$), from the observation of a fierce peak at ~1084 cm^{-1} along with tiny features at ~158 cm^{-1}, ~273 cm^{-1}, and ~713 cm^{-1}, which is related to the normal modes of the most stable polymorph of the calcium carbonate structure. Indeed, the strongest band of the spectrum, centered at ~1084 cm^{-1}, corresponds to the symmetric stretching of the CO_3 group, while the Raman peak at ~713 cm^{-1} can be ascribed to symmetric CO_3 deformation and the asymmetric stretching of the carbonate unit, respectively. Moreover, bands at ~158 cm^{-1} and ~273 cm^{-1} can be attributed to lattice vibrations involving translations and rotations of the carbonate groups within the crystal [60].

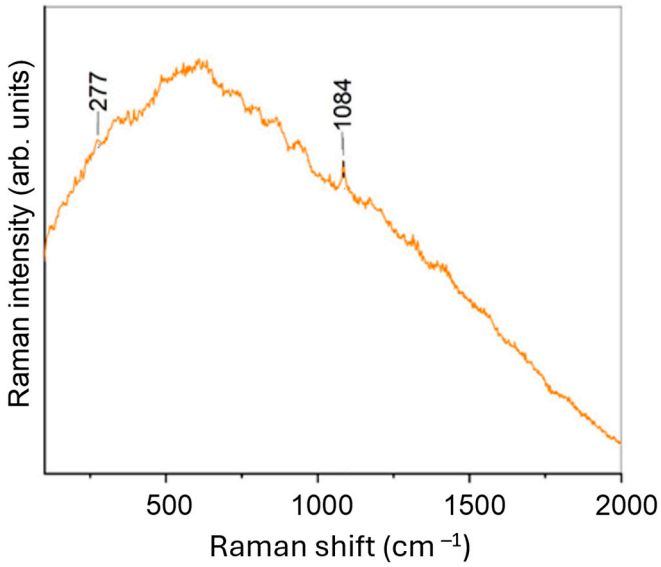

Figure 7. Representative micro-Raman spectrum recorded on "Comiso" stone.

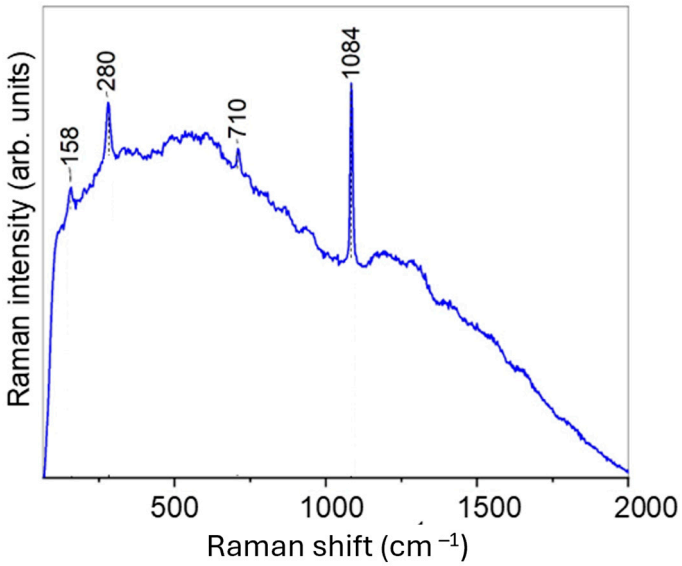

Figure 8. Representative micro-Raman spectrum recorded on "Mendicino" stone.

In addition, the micro-Raman spectrum for the "Comiso" stone as reported in Figure 7, again revealed a composition mainly based on calcite, from the observation of the peak at ~1084 cm^{-1}, along with a tiny feature at ~277 cm^{-1} [61].

Lastly, the micro-Raman profile of the "Mendicino" stone, shown in Figure 8, suggested a composition also mostly made of calcite, from the observation of a fierce peak at ~1084 cm^{-1}, along with tiny features at ~158 cm^{-1}, ~280 cm^{-1}, and ~710 cm^{-1} [62].

The MRS results are in very good agreement with the XRD ones. Both methods clearly identify the presence of calcite, whereas the MRS does not detect any significant amount of other mineralogical phases, probably due to the small laser spot size (25 μm), together with the intrinsic limitations of the MRS technique, which can only provide surface-level information.

5. Conclusions

The radon exhalation rate, the natural radioactivity content, and the mineralogy of natural stones of particular historical–artistic interest employed as building materials, i.e., the "Noto", "Comiso", and "Mendicino" samples, were investigated through a multi-

disciplinary approach by using the Closed Chamber Method (CCM) with the Durridge Rad7 apparatus for short-lived radon progeny alpha spectrometry, the HPGe gamma-ray spectrometry, XRD, and the MRS spectroscopy.

In particular, the activity concentrations of ^{226}Ra, ^{232}Th, and ^{40}K are significantly lower than the average world values for all the investigated stones. Moreover, in order to assess potential radiological hazards associated with radiation exposure from the analyzed specimens, D, ACI, and I_α were estimated. Specifically, D was found to be lower than the natural background value of 59 nGy h^{-1} in all cases. Furthermore, it was verified that ACI and I_α were less than unity, suggesting that there are negligible radiological risks connected to gamma radiation exposure and very little chance of exposure to indoor radon concentrations greater than 200 Bq m^{-3}.

Finally, the presence of calcite as the main mineral was identified in all stones by using XRD and micro-Raman spectroscopy. In addition, it is worth noting that the significant presence of any radioisotope-bearing minerals can be excluded by XRD and MRS analysis, in very good agreement with the very low level of natural radioactivity content measured in the investigated samples.

Author Contributions: Conceptualization, F.C. and V.V.; methodology, F.C.; validation, G.M. and D.M.; formal analysis, D.C., S.D.P., G.F. and M.G.; investigation, F.C., S.A.R. and V.V.; resources, F.C. and M.P.; data curation, F.C.; writing—original draft preparation, F.C.; supervision, D.M. and V.V. All authors have read and agreed to the published version of the manuscript.

Funding: This work was performed in the framework of the PRIN 2022 PNRR ATHENA (a novel approach toward the management of building materials of particular historical–artistic interest: assessment of the radon exhalation and the radiological risk due to natural radioactivity content) project, CUP J53D23014560001, funded by the European Union—Next Generation EU, PNRR—Mission 4, Component 2, Investment 1.1—PRIN 2022 PNRR Call for Proposals—Directorial Decree No. 1409 of 14 September 2022.

Institutional Review Board Statement: Not applicable.

Informed Consent Statement: Not applicable.

Data Availability Statement: Data are contained within the article.

Conflicts of Interest: The authors declare no conflicts of interest.

References

1. United Nations Scientific Committee on the Effects of Atomic Radiation. *Sources and Effects of Ionizing Radiation: Report to the General Assembly, with Scientific Annexes*; UNSCEAR: New York, NY, USA, 2000; Volume I, ISBN 92-1-142238-8.
2. Navas, A.; Soto, J.; Machín, J. 238U, 226Ra, 210Pb, 232Th and 40K activities in soil profiles of the Flysch sector (Central Spanish Pyrenees). *Appl. Radiat. Isot.* **2002**, *57*, 579–589. [CrossRef] [PubMed]
3. Caridi, F.; Di Bella, M.; Sabatino, G.; Belmusto, G.; Fede, M.R.; Romano, D.; Italiano, F.; Mottese, A.F. Assessment of Natural Radioactivity and Radiological Risks in River Sediments from Calabria (Southern Italy). *Appl. Sci.* **2021**, *11*, 1729. [CrossRef]
4. Caridi, F.; Messina, M.; Faggio, G.; Santangelo, S.; Messina, G.; Belmusto, G. Radioactivity, radiological risk and metal pollution assessment in marine sediments from Calabrian selected areas, Southern Italy. *Eur. Phys. J. Plus* **2018**, *133*, 65. [CrossRef]
5. Omar-Nazir, L.; Shi, X.; Moller, A.; Mousseau, T.; Byun, S.; Hancock, S.; Seymour, C.; Mothersill, C. Long-term effects of ionizing radiation after the Chernobyl accident: Possible contribution of historic dose. *Environ. Res.* **2018**, *165*, 55–62. [CrossRef]
6. Kamiya, K.; Ozasa, K.; Akiba, S.; Niwa, O.; Kodama, K.; Takamura, N.; Zaharieva, E.K.; Kimura, Y.; Wakeford, R. Long-term effects of radiation exposure on health. *Lancet* **2015**, *386*, 469–478. [CrossRef]
7. Jaafar, L.; Podolsky, R.H.; Dynan, W.S. Long-Term Effects of Ionizing Radiation on Gene Expression in a Zebrafish Model. *PLoS ONE* **2013**, *8*, e69445. [CrossRef]
8. Torrisi, L.; Caridi, F.; Giuffrida, L. Protons and ion acceleration from thick targets at 10^{10} W/cm^2 laser pulse intensity. *Las. and Part. Beams* **2011**, *29*, 29–37. [CrossRef]
9. WHO. *Indoor Radon a Public Health Perspective*; WHO: Geneva, Switzerland, 2007; 110p.
10. Al-Azmi, D.; Okeyode, I.C.; Alatise, O.O.; Mustapha, A.O. Setup and procedure for routine measurements of radon exhalation rates of building materials. *Radiat. Meas.* **2018**, *112*, 6–10. [CrossRef]
11. Nazaroff, W.W. *Radon and Its Decay Products in Indoor Air*; John Wiley and Sons, Incorporated: Hoboken, NJ, USA, 1988; ISBN 0-471-62810-7.

12. Amaral, P.G.Q.; Galembeck, T.M.B.; Bonotto, D.M.; Artur, A.C. Uranium distribution and radon exhalation from Brazilian dimension stones. *Appl. Radiat. Isot.* **2012**, *70*, 808–817. [CrossRef]
13. Estokova, A.; Singovszka, E.; Vertal, M. Investigation of Building Materials' Radioactivity in a Historical Building—A Case Study. *Materials* **2022**, *15*, 6876. [CrossRef]
14. Liu, C.; Benotto, M.; Ungar, K.; Chen, J. Environmental monitoring and external exposure to natural radiation in Canada. *J. Environ. Radioact.* **2022**, *243*, 106811. [CrossRef] [PubMed]
15. Stoulos, S.; Manolopoulou, M.; Papastefanou, C. Assessment of natural radiation exposure and radon exhalation from building materials in Greece. *J. Environ. Radioact.* **2003**, *69*, 225–240. [CrossRef]
16. Righi, S.; Bruzzi, L. Natural radioactivity and radon exhalation in building materials used in Italian dwellings. *J. Environ. Radioact.* **2006**, *88*, 158–170. [CrossRef] [PubMed]
17. Caridi, F.; Torrisi, L.; Margarone, D.; Borrielli, L. Investigations on low temperature laser-generated plasmas. *Las. Part. Beams* **2008**, *26*, 265–271. [CrossRef]
18. Bonardi, G.; De Capoa, P.; Fioretti, B.; Perrone, V. Some remarks on the Calabria-Peloritani arc and its relationship with the Southern Apennines. *Boll. Geofis. Teor. Appl.* **1994**, *XXXVI*, 483–492.
19. Saleh, E.E.; Al-Sobahi, A.M.A.; El-Fiki, S.A.E. Assessment of radon exhalation rate, radon concentration and annual effective dose of some building materials samples used in Yemen. *Acta Geophys.* **2021**, *69*, 1325–1333. [CrossRef]
20. Zhang, L.; Lei, X.; Guo, Q.; Wang, S.; Ma, X.; Shi, Z. Accurate measurement of the radon exhalation rate of building materials using the closed chamber method. *J. Radiol. Prot.* **2012**, *32*, 315–323. [CrossRef]
21. Anania, L.; Badalà, A.; Barone, G.; Belfiore, C.; Calabrò, C.; La Russa, M.; Mazzoleni, P.; Pezzino, A. The stones in monumental masonry buildings of the "Val di Noto" area: New data on the relationships between petrographic characters and physical-mechanical properties. *Constr. Build. Mater.* **2012**, *33*, 122–132. [CrossRef]
22. Comite, V.; Álvarez de Buergo, M.; Barca, D.; Belfiore, C.M.; Bonazza, A.; La Russa, M.F.; Pezzino, A.; Randazzo, L.; Ruffolo, S.A. Damage monitoring on carbonate stones: Field exposure tests contributing to pollution impact evaluation in two Italian sites. *Constr. Build. Mater.* **2017**, *152*, 907–922. [CrossRef]
23. Ruffolo, S.A.; La Russa, M.F.; Ricca, M.; Belfiore, C.M.; Macchia, A.; Comite, V.; Pezzino, A.; Crisci, G.M. New insights on the consolidation of salt weathered limestone: The case study of Modica stone. *Bull. Eng. Geol. Environ.* **2017**, *76*, 11–20. [CrossRef]
24. Olivetti, V.; Cyr, A.J.; Molin, P.; Faccenna, C.; Granger, D.E. Uplift history of the Sila Massif, southern Italy, deciphered from cosmogenic 10Be erosion rates and river longitudinal profile analysis. *Tectonics* **2012**, *31*, TC3007. [CrossRef]
25. Forestieri, G.; Alvarez de Buergo, M. Relationships Between Petrophysical and Mechanical Properties of Certain Calcarenites Used in Building. *Geotech. Geol. Eng.* **2021**, *39*, 5021–5040. [CrossRef]
26. Tuccimei, P.; Mollo, S.; Soligo, M.; Scarlato, P.; Castelluccio, M. Real-time setup to measure radon emission during rock deformation: Implications for geochemical surveillance. *Geosci. Instrum. Methods Data Syst.* **2015**, *4*, 111–119. [CrossRef]
27. Alhamdi, W.A.; Abdullah, K.M.S. Determination of Radium and Radon Exhalation Rate as a Function of Soil Depth of Duhok Province—Iraq. *J. Radiat. Res. Appl. Sci.* **2021**, *14*, 486–494. [CrossRef]
28. Čeliković, I.; Pantelić, G.; Vukanac, I.; Nikolić, J.K.; Živanović, M.; Cinelli, G.; Gruber, V.; Baumann, S.; Ciotoli, G.; Poncela, L.S.Q.; et al. Overview of Radon Flux Characteristics, Measurements, Models and Its Potential Use for the Estimation of Radon Priority Areas. *Atmosphere* **2022**, *13*, 2005. [CrossRef]
29. Tuccimei, P.; Moroni, M.; Norcia, D. Simultaneous determination of ^{222}Rn and ^{220}Rn exhalation rates from building materials used in Central Italy with accumulation chambers and a continuous solid state alpha detector: Influence of particle size, humidity and precursors concentration. *Appl. Radiat. Isot.* **2006**, *64*, 254–263. [CrossRef]
30. Mancini, S.; Caliendo, E.; Guida, M.; Bisceglia, B. Preliminary assessment, by means of Radon exhalation rate measurements, of the bio-sustainability of microwave treatment to eliminate biodeteriogens infesting stone walls of monumental historical buildings. *IOP Conf. Ser. Mater. Sci. Eng.* **2017**, *251*, 012026. [CrossRef]
31. Caridi, F.; Testagrossa, B.; Acri, G. Elemental composition and natural radioactivity of refractory materials. *Environ. Earth Sci.* **2021**, *80*, 170. [CrossRef]
32. Caridi, F.; Messina, M.; Belvedere, A.; D'Agostino, M.; Marguccio, S.; Settineri, L.; Belmusto, G. Food salt characterization in terms of radioactivity and metals contamination. *Appl. Sci.* **2019**, *9*, 2882. [CrossRef]
33. Eckert-Ziegler Calibration Sources. 2020. Available online: https://www.ezag.com/home/products/ (accessed on 21 October 2024).
34. Ortec GammaVision®, version 8; 2023. Available online: https://www.htds.fr/wp-content/uploads/2019/04/GammaVision-version-8-4.pdf (accessed on 24 October 2024).
35. Harb, S.; Din, K.S.; Abbady, A.; Mostafa, M. Activity Concentration for Surface Soil Samples Collected From Armant, Qena, Egypt. In Proceedings of the EPC'10: 4th Environmental Physics Conference, Hurghada, Egypt, 10–14 March 2010; pp. 49–57.
36. Guidotti, L.; Carini, F.; Rossi, R.; Gatti, M.; Cenci, R.M.; Beone, G.M. Gamma-spectrometric measurement of radioactivity in agricultural soils of the Lombardia region, northern Italy. *J. Environ. Radioact.* **2015**, *142*, 36–44. [CrossRef]
37. ACCREDIA. Available online: https://www.accredia.it/ (accessed on 28 October 2024).
38. Kotrappa, P.; Stieff, L. Application of NIST ^{222}Rn Emanation Standards for Calibrating ^{222}Rn Monitors. *Radiat. Prot. Dosim.* **1994**, *55*, 211–218. [CrossRef]
39. EC (European Commission). *Radiation Protection 112: Radiological Protection Principles Concerning the Natural Radioactivity of Building Materials*; EC (European Commission): Brussels, Belgium, 1999; pp. 1–16.

40. Presidenza del Consiglio dei Ministri. Legislation Italian D. Lgs. 101/20. 2020. Available online: https://www.normattiva.it/atto/caricaDettaglioAtto?atto.dataPubblicazioneGazzetta=2020-08-12&atto.codiceRedazionale=20G00121&atto.articolo.numero=0&atto.articolo.sottoArticolo=1&atto.articolo.sottoArticolo1=0&qId=111072d7-345b-4ffe-b64c-7dde4438f2e4&tabID=0.6991185232046224&title=lbl.dettaglioAtto (accessed on 21 October 2024).
41. Kotrappa, P.; Jester, W.A. Electret ion chamber radon monitors measure dissolved ^{222}Rn in water. *Health Phys.* **1993**, *64*, 397–405. [CrossRef] [PubMed]
42. Alghamdi, A.S.; Aleissa, K.; Al-Hamarneh, I. Gamma radiation and indoor radon concentrations in the western and southwestern regions of Saudi Arabia. *Heliyon* **2019**, *5*, e01133. [CrossRef] [PubMed]
43. Malvern Panalytical. *Empyrean Diffractometer User Manual*; Malvern Panalytical: Malvern, UK, 2013.
44. Gruber, V.; Bossew, P.; De Cort, M.; Tollefsen, T. The European map of the geogenic radon potential. *J. Radiol. Prot.* **2013**, *33*, 51. [CrossRef] [PubMed]
45. BW TEK BTR 111 Mini-RamTM Datasheet. 2019. Available online: https://bwtek.com/products/raman-systems/ (accessed on 22 October 2024).
46. Torrisi, L.; Margarone, D.; Borrielli, A.; Caridi, F. Ion and photon emission from laser-generated titanium-plasma. *Appl. Surf. Sci.* **2008**, *254*, 4007–4012. [CrossRef]
47. Markkanen, M. *Radiation Dose Assessments for Materials with Elevated Natural Radioactivity*; Finnish Centre for Radiation and Nuclear Safety (STUK): Helsinki, Finland, 1995; Volume 2, ISBN 9517120796.
48. UNSCEAR. *United Nations Scientific Committee on the Effects of Atomic Radiation, Vol. I, Annex B: Exposure of the Public and Workers from Various Sources of Radiation*; United Nations: New York, NY, USA, 2008.
49. Avwiri, G.O.; Egieya, J.M. Radiometric assay of hazard indices and excess lifetime cancer risk due to natural radioactivity in soil profile in Ogba/Egbema/Ndoni local government area of Rivers state, Nigeria. *Acad. Res. Int.* **2013**, *4*, 54–65.
50. Scharfenberg, L.; Regelous, A.; de Wall, H. Radiogenic heat production of Variscan granites from the Western Bohemian Massif, Germany. *J. Geosci.* **2020**, *64*, 251–269. [CrossRef]
51. Pietrzak, U.; McPhail, D.C. Copper accumulation, distribution and fractionation in vineyard soils of Victoria, Australia. *Geoderma* **2004**, *122*, 151–166. [CrossRef]
52. Nuccetelli, C.; Risica, S.; D'Alessandro, M.; Trevisi, R. Natural radioactivity in building material in the European Union: Robustness of the activity concentration index I and comparison with a room model. *J. Radiol. Prot.* **2012**, *32*, 349. [CrossRef]
53. Stumpo, S. *The Sustainability of Urban Heritage Preservation The Case of Siracusa, Italia*; Inter-American Development Bank: Washington, DC, USA, 2010; pp. 1–32.
54. Gunasekaran, S.; Anbalagan, G.; Pandi, S. Raman and Infrared Spectra of Carbonates of Calcite Structure. *J. Raman Spectrosc.* **2006**, *37*, 892–899. [CrossRef]
55. Pyle, D.; Blatt, H.; Tracy, R.J. Petrology. Igneous, Sedimentary, and Metamorphic, 2nd ed. xix + 529 pp. New York, Basingstoke: W. H. Freeman & Co. Price £34.95, US $64.95 (hard covers). ISBN 0 7167 2438 3. *Geol. Mag.* **1997**, *134*, 121–142. [CrossRef]
56. Decarlo, T.; Gaetani, G.; Holcomb, M.; Cohen, A. Experimental determination of factors controlling U/Ca of aragonite precipitated from seawater: Implications for interpreting coral skeleton. *Geochim. Cosmochim. Acta* **2015**, *162*, 151–165. [CrossRef]
57. Finch, R.; Murakami, T. Uranium in the environment: Mineralogy, geochemistry and the radiochemical cycle. *Rev. Mineral. Geochem.* **1999**, *38*, 91–179.
58. Langmuir, D. Uranium solution-mineral equilibria at low temperatures with applications to sedimentary ore deposits. *Geochim. Cosmochim. Acta* **1978**, *42*, 547–569. [CrossRef]
59. Ivanovich, M.; Harmon, R.S. *Uranium-Series Disequilibrium: Applications to Earth, Marine, and Environmental Sciences*, 2nd ed.; Clarendon Press: Oxford, UK, 1992; ISBN 019854278X.
60. Weththimuni, M.L.; Licchelli, M.; Malagodi, M.; Rovella, N.; La Russa, M. Consolidation of bio-calcarenite stone by treatment based on diammonium hydrogenphosphate and calcium hydroxide nanoparticles. *Meas. J. Int. Meas. Confed.* **2018**, *127*, 396–405. [CrossRef]
61. Spoto, S.E.; Paladini, G.; Caridi, F.; Crupi, V.; D'Amico, S.; Majolino, D.; Venuti, V. Multi-Technique Diagnostic Analysis of Plasters and Mortars from the Church of the Annunciation (Tortorici, Sicily). *Materials* **2022**, *15*, 958. [CrossRef]
62. Briani, F.; Caridi, F.; Ferella, F.; Gueli, A.M.; Marchegiani, F.; Nisi, S.; Paladini, G.; Pecchioni, E.; Politi, G.; Santo, A.P.; et al. Multi-Technique Characterization of Painting Drawings of the Pictorial Cycle at the San Panfilo Church in Tornimparte (AQ). *Appl. Sci.* **2023**, *13*, 6492. [CrossRef]